

and one result is the statistical "blip" in 1956 (Fig. 2). Between 1952 and 1962, first professional degrees were subtracted from all BA degrees to achieve maximum comparability with later years.

3. P. M. Seigal and R. Bruno, *School Enrollment—Social and Economic Characteristics of Students October 1982* (U.S. Bureau of the Census, *Curr Popul. Rep. Ser. P-20, No. 408*, Government Printing Office, Washington, DC, 1986), table A-4.
4. Other demographic variables were also considered. Specifically, neither the age profile of the student population nor its racial or ethnic composition correlate closely with the AS share [*Curr Popul. Rep. Ser. P-20*, October 1982, tables A-3 and A-4; National Center for Education Statistics, *The Condition of Education*, 1989, vol. 2, tables 2.5-3 and 2.6-1].
5. J. B. Lon Hefferlin, *Dynamics of Academic Reform* (Jossey-Bass, San Francisco, 1971), especially chapter 3.
6. More complete data for the major sectors of higher education document this proposition [table 4.3 in (1), p. 56].
7. We define AS share for men as the percentage of all BA degrees earned by men that were awarded in the arts and sciences; we do not mean the percentage of all degrees in the arts and sciences that were earned by men rather than by women. Similarly,

the humanities share for men is the percentage of all BA degrees earned by men that were awarded in the humanities.

8. The total AS share is related to the gender-specific shares as follows.

$$AS_T = AS_M R_M + AS_W(1 - R_M)$$

where AS_T is the total AS share; AS_M is the share for men; R_M is the percentage of all degrees awarded to men; and AS_W is the AS share for women.

9. Engineering is the other large field outside the arts and sciences, but it has been important quantitatively only for men; in 1986, the engineering share for women was still only 2.5%. Nursing is another field in which women have sought degrees, and the nursing share of all BA degrees for women rose from about 3% in 1970 to a peak of 6.7% in 1980—largely as a result of the increasing technical sophistication of the field and the associated tendency for BA programs to replace certificate programs.
10. We thank L. Cremin and L. Stone, as well as N. Rudenstine, H. Zuckerman, and other colleagues at the Foundation too numerous to mention individually, for helpful comments on drafts of this paper. Also, we thank K. Motihar and P. McNeil for assistance in assembling data for the six case-study institutions.

Scattering and Recoiling Spectrometry: An Ion's Eye View of Surface Structure

J. WAYNE RABALAIS

Recent developments in ion-scattering spectrometry have led to a surface crystallography that is sensitive to all elements, including hydrogen. Time-of-flight techniques for the detection of atoms scattered and recoiled from surfaces in simple collision sequences, together with calculations of shadowing and blocking cones, can be used to make direct measurements of interatomic spacings and adsorption sites within an accuracy of ≈ 0.1 angstrom. Time-of-flight detection of both neutrals and ions provides the high sensitivity necessary for nondestructive analysis. Structures are determined by monitoring the angular anisotropies in the scattered primary and recoiled target atom flux. Such surface and adsorption site determinations find application in such fields as catalysis, thin film growth, and interfaces.

SCATTERING EXPERIMENTS HAD THEIR ORIGINS IN THE DEVELOPMENT of modern atomic theory at the beginning of this century. As a result of both the Rutherford experiment on the scattering of alpha particles (He nuclei) by thin metallic foils and the Bohr theory of atomic structure, a consistent model of the atom as a small massive nucleus surrounded by a large swarm of light electrons was confirmed. It was quickly realized that the inverse process, namely, analysis of the scattering pattern of ions from crystals, could provide information on composition and structure. This analysis is straightforward because the kinematics of energetic atomic collisions is accurately described by classical mechanics. Such scattering occurs as a result of the mutual Coulomb repulsion between the colliding

atomic cores, that is, the nucleus plus core electrons. The scattered primary atom loses some of its energy to the target atom. The latter, in turn, recoils into a forward direction. The final energies of the scattered and recoiled atoms and the directions of their trajectories are determined by the masses of the pair of atoms involved and the closeness of the collision. By analysis of these final energies and the angular distributions of the scattered and recoiled atoms, the elemental composition and structure of the surface can be deciphered.

Ion-scattering spectrometry (ISS) with ion energies in the low kiloelectron volt range is the surface-sensitive analog of Rutherford backscattering spectrometry (RBS) (1). RBS is sensitive to long-range bulk structure through the use of ions in the million electron volt range. ISS as a surface analysis technique developed rapidly after the 1967 work of Smith (2), which demonstrated surface elemental analysis. Interest in ISS as a technique for investigating surface structure grew quickly after the 1982 work of Aono *et al.* (3), which showed that the use of backscattering angles near 180° greatly simplified the scattering geometry and interpretation. In 1984, Buck and his associates (4) demonstrated the high sensitivity of time-of-flight (TOF) detection of scattered particles for structural analysis. The recent coupling (5) of TOF methods with detection of both scattered and recoiled particles has led to the development of time-of-flight scattering and recoiling spectrometry (TOF-SARS) as a tool for structural analysis. Several research groups (6-16) throughout the world are now engaged in surface structure determinations using some form of kiloelectron volt ISS.

Basic Physics Underlying TOF-SARS

Two basic physical phenomena govern atomic collisions in the kiloelectron volt range. First, repulsive interatomic interactions, described by the laws of classical mechanics, control the scattering

The author is in the Department of Chemistry, University of Houston, Houston, TX 77204.

and recoiling trajectories. Second, electronic transition probabilities, described by the laws of quantum mechanics, control the ion-surface charge exchange process.

Atomic collisions in the kiloelectron volt range. The dynamics of kiloelectron volt atomic collisions are well described as binary collisions between the incident ion and surface atoms (17). When an

energetic ion makes a direct collision with a surface atom, the surface atom recoils into a forward direction, as shown in Fig. 1. Both the scattered and recoiled atoms have high, discrete kinetic energy distributions. According to the laws of conservation of energy and momentum, the TOF of an incident ion of mass M_1 and energy E_0 that is scattered from a target atom of mass M_2 into an angle θ is given by

$$t_S = L(M_1 + M_2)/(2M_1E_0)^{1/2}\{\cos \theta + [(M_2/M_1)^2 - \sin^2 \theta]^{1/2}\} \quad (1)$$

where L is the flight distance, that is, the distance from target to detector. For cases where $M_1 > M_2$, there is a critical angle $\theta_c = \sin^{-1}(M_2/M_1)$ above which only multiple scattering can occur. Recoils that are ejected from single collisions of the projectile into an angle ϕ , that is, direct recoils, have a TOF given by

$$t_R = L(M_1 + M_2)/(8M_1E_0)^{1/2} \cos \phi \quad (2)$$

As a result of the energetic nature of the collisions, only atomic species are observed as direct recoils, and their energies are independent of the chemical bonding environment.

Interatomic potentials. Although scattering in the kiloelectron volt range is dominated by repulsive potentials, it is not simply a hard sphere or billiard ball collision, where there is a clean "hit" or "miss." The partial penetration of the ion into the target atom's electron cloud results in bent trajectories even when there is not a "head-on" collision. This type of interaction is well described by a screened Coulomb potential (17) such as

$$V(r) = [Z_1Z_2e^2/R]\phi(R/CR_s) \quad (3)$$

where R is the internuclear separation and the Z_i are the atomic numbers of the collision partners; ϕ is a screening function that is determined by R , the screening radius R_s , and a scaling parameter

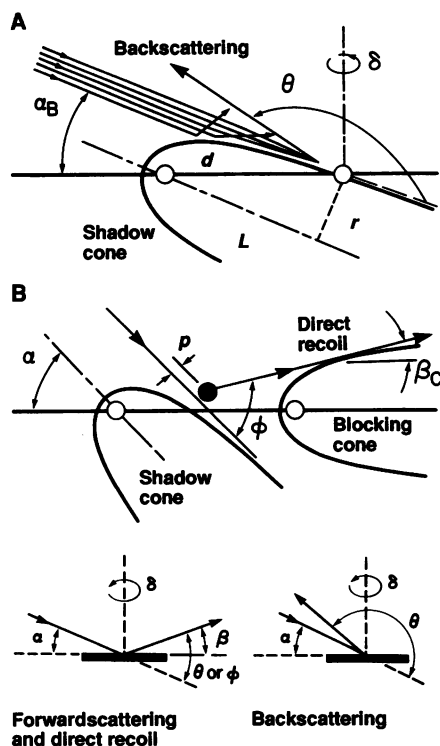


Fig. 1. Schematic illustrations of (A) backscattering and shadowing and (B) direct recoiling with shadowing and blocking. The angular notation is defined in the lower part of the diagram; α_B , incident ion angle.

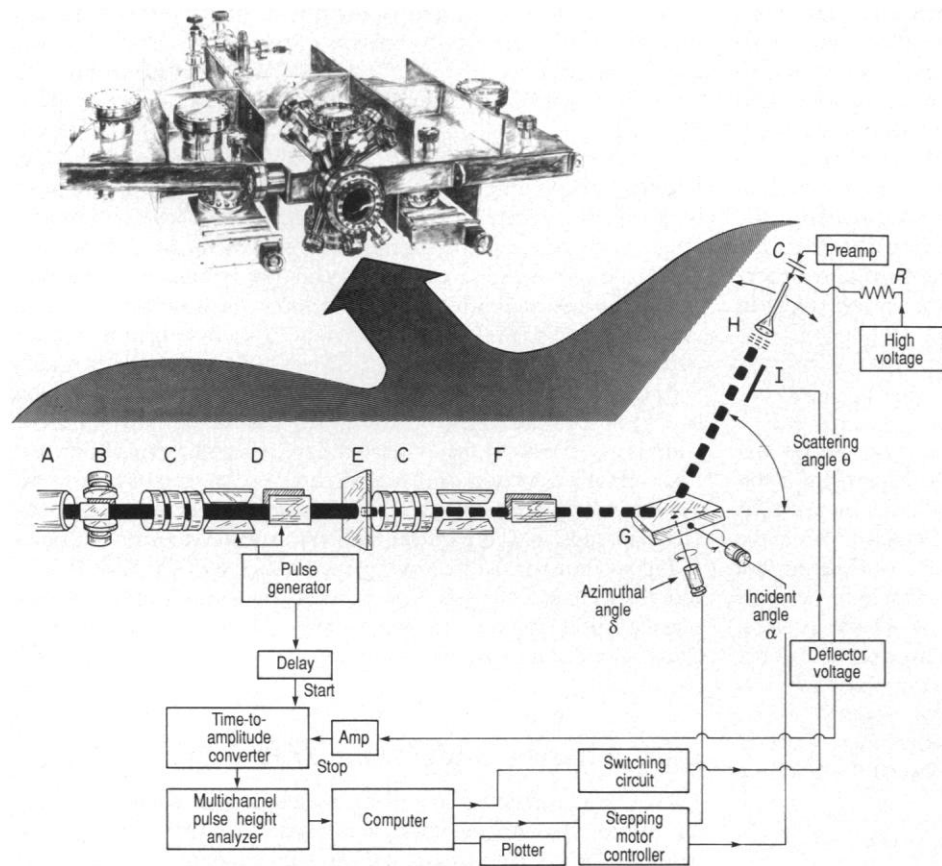


Fig. 2. TOF-SARS spectrometer system with schematic drawing of the vacuum chamber. Abbreviations: A, ion gun; B, Wien filter; C, Einzel lens; D, pulsing plates; E, pulsing aperture; F, deflector plates; G, sample; H, electron multiplier detector with energy prefilter grid; I, electrostatic deflector; R, resistor; and C, capacitor.

C; there are several good approximations for ϕ (17). Using such a potential, one can determine the relation between the scattering angle θ and the impact parameter p . The p is defined as the minimum perpendicular distance from the target atom to the ion trajectory. A small value of p corresponds to a near head-on collision and backscattering, and a large value corresponds to a glancing collision and forwardscattering. Similarly, the recoiling angle ϕ is also determined by p .

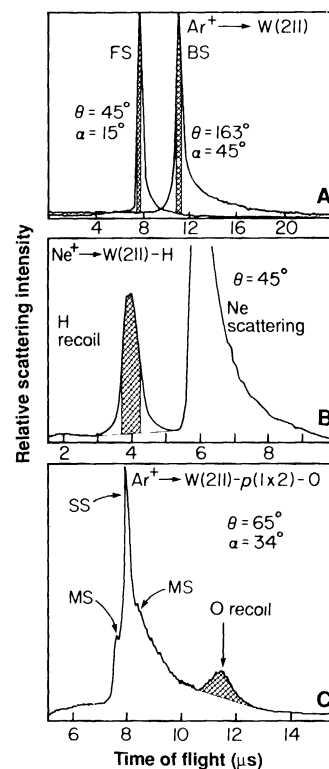
Shadowing and blocking cones. Considering a large number of ions with parallel trajectories impinging on a target atom, the ion trajectories are bent by the repulsive potential such that there is an excluded volume, called the shadow cone, in the shape of a paraboloid formed behind the target atom as shown in Fig. 1. Ion trajectories do not penetrate into the shadow cone but instead are concentrated at its edges, in much the way that rain pours off an umbrella. Atoms located inside the cone behind the target atom are shielded from the impinging ions. Similarly, if the scattered ion or recoiling atom trajectory is directed toward a neighboring atom, that trajectory will be blocked. For a large number of scattering or recoiling trajectories, a blocking cone will be formed behind the neighboring atom into which no particles can penetrate.

The dimensions of the shadowing and blocking cones can be determined experimentally from scattering measurements along crystal azimuths for which the interatomic spacings are accurately known. This provides an experimental determination of C and reliable cone dimensions. The cone dimensions can also be constructed theoretically from the relation of p with θ and ϕ (17, 18). A universal shadow cone curve has been proposed (19), and cone dimensions for common ion-atom combinations have been reported (20). Because the radii of these cones are of the same order as interatomic spacings, that is, 1 to 2 Å, the ions penetrate only into the outermost surface layers.

Scattering and recoiling anisotropy caused by shadowing and blocking cones. When an isotropic ion fluence impinges on a crystal surface at a specific incident angle α , the scattered and recoiled atom flux is anisotropic. This anisotropy is a result of the incoming ion's eye view of the surface, which depends on the specific arrangement of atoms and the shadowing and blocking cones. The arrangement of atoms controls the atomic density along the azimuths and the ability of ions to channel, that is, to penetrate into empty spaces between atomic rows. The cones determine which nuclei are screened from the impinging ion flux and which exit trajectories are blocked. By measuring the ion and atom flux at specific scattering and recoiling angles as a function of ion beam incident α and azimuthal δ angles to the surface, one can observe structures that can be interpreted in terms of the interatomic spacings and shadow cones from the ion's eye view. The anisotropy in the scattered and recoiled flux is best observed in scattering and recoiling structural contour maps, which are plots of the scattered or recoiled intensity in α, δ -space.

Ion-surface electronic transitions. Electron exchange (21) between ions or atoms and surfaces can occur in two regions: in region 1, along the incoming and outgoing trajectories where the particle is within angstroms of the surface, and in region 2, in the close atomic encounter where the core electron orbitals of the collision partners overlap. In region 1, the dominating processes are resonant and Auger electron tunneling transitions, both of which are fast ($\tau < 10^{-15}$ s). Since the work functions of most solids are lower than the ionization potentials of most gaseous atoms, kiloelectron volt scattered and recoiled species are predominantly neutrals as a result of electron capture from the solid. In region 2, as the interatomic distance R decreases, the atomic orbitals (AOs) of the separate atoms of atomic number Z_1 and Z_2 evolve into molecular orbitals (MOs) of a quasi-molecule and finally into the AO of the "united" atom of atomic number ($Z_1 + Z_2$). As R decreases, a

Fig. 3. TOF spectra for 4-keV Ar^+ scattering from (A) clean W(211) and from (C) the O-chemisorbed W(211) surface and (B) 4-keV Ne^+ scattering from the H-chemisorbed W(211) surface. FS, forwardscattering; BS, backscattering; SS, single scattering collisions; MS, multiple scattering collisions.



critical distance is reached at which electrons are promoted into higher energy MOs because of electronic repulsion and the Pauli exclusion principle. This can result in collisional reionization of neutral species. The fraction of species scattered and recoiled as ions is sensitive to atomic structure through changes in electron density along the trajectories.

TOF-SARS Instrumentation

An instrument for structural studies by ion scattering and recoiling should be capable of continuous variation of the scattering θ , beam incident α , and crystal azimuthal δ angles (see Fig. 1), generation of a pulsed kiloelectron volt primary ion beam of low fluence, efficient detection of both ions and neutrals, in situ low-energy electron diffraction (LEED), and operation in an ultrahigh-vacuum ($<10^{-10}$ torr) environment. Figure 2 illustrates the TOF-SARS constructed at the University of Houston (22). The primary ion beam is a 1- to 5-keV rare gas ion source, which has a narrow energy spread, is mass-selected, is pulsed at 10 to 40 kHz with pulse widths of 20 to 50 ns for an average ion current density of <1 nA/cm², and has low angular divergence. The detector is a channel electron multiplier or channel plate that is sensitive to both ions and fast neutrals. The sample is mounted on a precision manipulator, and the angles α and δ are computer-controlled by means of stepping motors. The velocities of the scattered and recoiled particles are analyzed by measuring their flight times from the sample to detector, a distance of 1 m. An electrostatic deflector plate near the flight path allows deflection of ions for the collection of TOF spectra of neutrals as compared to that of ions plus neutrals. Standard timing electronics are used for data collection. TOF spectra can be collected with a dose of $<10^{-3}$ ions per surface atom, making the technique relatively nondestructive. The system also has ports that contain standard surface analysis techniques such as LEED, Auger electron spectroscopy (AES), and x-ray photoelectron spectroscopy (XPS).

Elemental Analysis from TOF-SARS

TOF-SARS is capable of detecting all elements by either scattering, recoiling, or both techniques. TOF peak identification is straightforward by application of Eqs. 1 and 2. Collection of neutrals plus ions results in scattering and recoiling intensities that are determined by elemental concentrations, shadowing and blocking effects, and classical cross sections.

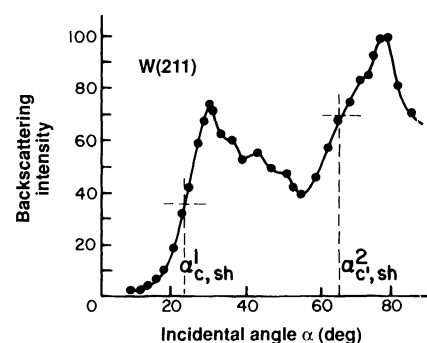
TOF spectra. Spectra from a clean tungsten surface and from O and H chemisorbed on that surface are shown in Fig. 3. For clean W(211), both the backscattering (BS) and forwardscattering (FS) spectra have sharp peaks at the TOF positions predicted by Eq. 1. The absence of H, C, and O recoils in the FS spectrum indicates that the surface is clean and free of the normal atmospheric contaminants, and specifically that it has <1% of a monolayer (ML) of these contaminants. The high background on the long TOF side of the peaks is attributable to ions that have lost energy because of multiple collisions and penetration. When O is chemisorbed on W(211), an O recoil peak O(R) is observed in the TOF spectrum at the position predicted by Eq. 2. The O(R) peak is on the long TOF side of the Ar⁺ scattering peak. As the scattering angle θ is reduced to smaller values, the recoil peak shifts toward lower TOF until it appears on the low TOF side of the scattering peak. Such a case is shown for H chemisorbed on W(211), where the probe was a Ne⁺ beam. One obtains the intensities necessary for structural analysis by integrating the areas of fixed time windows under these peaks.

Structural Analysis from TOF-SARS

The atomic structure of a surface is usually not a simple termination of the bulk structure. A classification exists based on the relation of surface to bulk structure. A bulk truncated surface has a structure identical to that of the bulk. A relaxed surface has the symmetry of the bulk structure but different interatomic spacings. With respect to the first and second layers, lateral relaxation refers to shifts in layer registry and vertical relaxation refers to shifts in layer spacings. A reconstructed surface has a symmetry different from that of the bulk symmetry. TOF-SARS provides "real space" information on the relative positions of all atoms in the surface region based on the classical concepts of shadowing and blocking cones. The cone dimensions can be calculated or calibrated from known interatomic spacings, and the analyses are not complicated by ion neutralization effects. The methods of structural analysis will be delineated below.

Backscattering versus incident angle α scans. When an ion beam is incident on an atomically flat surface at grazing angles, each surface atom is shadowed by its neighboring atom such that only FS is possible; these are large impact parameter (p) collisions. As α increases in this shadowing mode, a critical value $\alpha_{c,sh}^1$ is reached each time the i th layer of target atoms moves out of the shadow cone, allowing for large angle BS or small p collisions. If the BS intensity $I(BS)$ is monitored as a function of α , steep rises with well-defined maxima are observed when the focused trajectories at the edge of the shadow cone pass close to the center of neighboring atoms (Fig. 4). From the shape of the shadow cone [the radius (r) as a function of distance (ℓ) behind the target atom (Fig. 1)], the interatomic spacing (d) can be directly determined from plots of $I(BS)$ versus α . For example, by measuring $\alpha_{c,sh}^1$ along directions for which specific crystal azimuths are aligned with the projectile direction and using $d = r/\sin \alpha_{c,sh}^1$, one can determine interatomic spacings in the first atomic layer. The spacing between the first and second layers can be obtained in a similar manner from $\alpha_{c,sh}^2$ measured along directions for which the first- and second-layer

Fig. 4. Representative plot of $I(BS)$ versus α along the $[\bar{1}11]$ azimuth of W(211), using 4-keV Ar⁺.



atoms are aligned, providing a measure of the vertical relaxation in the outermost layers.

Backscattering versus azimuthal angle δ scans. Fixing the incident beam angle α and rotating the crystal about the surface normal while monitoring $I(BS)$ provides a scan of the crystal azimuthal angles δ . Such scans reveal the symmetry of the crystal structure. For example, one can obtain the azimuthal alignment and symmetry of the outermost layer by using a low α value such that scattering occurs from only the first atomic layer. With higher α values, similar information can be obtained for the second atomic layer. One can detect shifts in the first layer–second layer registry by carefully monitoring the $\alpha_{c,sh}^2$ values for second-layer scattering along directions near those azimuths for which the second-layer atoms are expected, from the bulk structure, to be directly aligned with the first-layer atoms. The $\alpha_{c,sh}^2$ values will be maximum for those δ values for which the first- and second-layer neighboring atoms are aligned.

Scattering structural contour map (SSCM). Data from the α and δ scans can be plotted together in the form of a contour map of the $I(BS)$ values in α, δ -space. Such a SSCM for the clean W(211) surface is shown in Fig. 5 along with a model of the surface structure. The SSCM provides the following information. (i) It reveals the symmetry of the $I(BS)$ data in α, δ -space, thereby providing a fingerprint for a specific crystal face and type with minor perturbations due to relaxation and possible major perturbations due to reconstruction. (ii) It shows what general regions of α, δ -space contain interesting structures for more detailed investigation. (iii) Comparison of the clean-surface SSCM to that of the adsorbate-covered surface provides a qualitative determination of the adsorbate sites and detection of any adsorbate-induced reconstruction or relaxation.

Consider the details of Fig. 5. The $\alpha_{c,sh}^1$ line at low α (Fig. 5B) corresponds to shadowing of first-layer atoms by their first-layer neighbors; this line is symmetrical about $\delta = 0^\circ$, as is the first atomic layer. It is consistent with first-layer interatomic spacings corresponding to the bulk truncated W(211) structure, showing that the surface is not reconstructed. Intense structures are observed at higher α resulting from subsurface-layer scattering; the intense peaks are due to focusing of ion trajectories by first- and second-layer W atoms onto third- and fourth-layer W atoms and back out again. The asymmetry about $\delta = 0^\circ$ is a result of the lack of symmetry between the first and underlying layers. The diagonal orientation of the line of intense peaks observed at higher α results from the fact that focusing onto subsurface layers for $\delta < 0^\circ$ occurs mainly at low α , while, for $\delta > 0^\circ$, this focusing occurs only at high α .

Forwardscattering versus azimuthal angle δ scans. When the scattering angle θ is decreased to a forward angle ($<90^\circ$), both shadowing effects along the incoming trajectory and blocking effects along the outgoing trajectory contribute to $I(FS)$ patterns. The blocking effects arise because the exit angle $\beta = \theta - \alpha$ is small at high α values. The features of plots of $I(FS)$ versus δ , with constant α and θ ,

are determined by shadowing and blocking along the close-packed azimuths. Surface periodicity can be read directly from these features (23), as shown in Fig. 6 for Pt(110). Minima are observed at the δ positions corresponding to alignment of the beam along specific azimuths. These minima are a result of shadowing and blocking along the close-packed directions, thus providing a direct reading of the surface periodicity.

Relaxation of the W(211) surface. From details of the above measurements (24, 25), it was determined that the W(211) surface had the symmetry of the bulk structure and, therefore, was not reconstructed. Careful analysis, however, showed that the surface interatomic spacings were different from those of the bulk structure, indicating that the surface was relaxed. The first layer–second layer registry, or lateral relaxation, was obtained from the determination of the $\alpha_{c,sh}$ maximum near the position expected for alignment of the first and second layers. The result shows that the lateral spacing from a second-layer atom to a first-layer atom along the $[1\bar{1}\bar{1}]$ azimuth shifts by 4% from that of the bulk truncated surface. This shift brings the center of the first-layer atoms nearer to the symmetrical bridge position between two second-layer atoms. The first layer–second layer spacing, or vertical relaxation, was determined from the $I(BS)$ versus α scans along those azimuths δ where the first- and second-layer atoms are aligned. The result shows that the vertical spacing between the two outermost layers is contracted by 9% from that of the bulk truncated surface (25).

Recoiling versus incident angle α scans. Adsorbates can be efficiently detected if they are recoiled into FS angles ϕ as shown in Figs. 1 and 7. As α increases, the adsorbate atoms move out of their neighboring atom shadow cones so that direct collisions from incident ions are possible. When the p value necessary for recoiling of the adsorbate atom into a specific ϕ becomes possible in a single collision, adsorbate recoils are observed with the TOF predicted from Eq. 2. Focusing at the edge of the shadow cone produces sharp rises in $I(R)$ as a function of α . By measuring $\alpha_{c,sh}$ corresponding to the recoil event, we can directly determine the interatomic distance

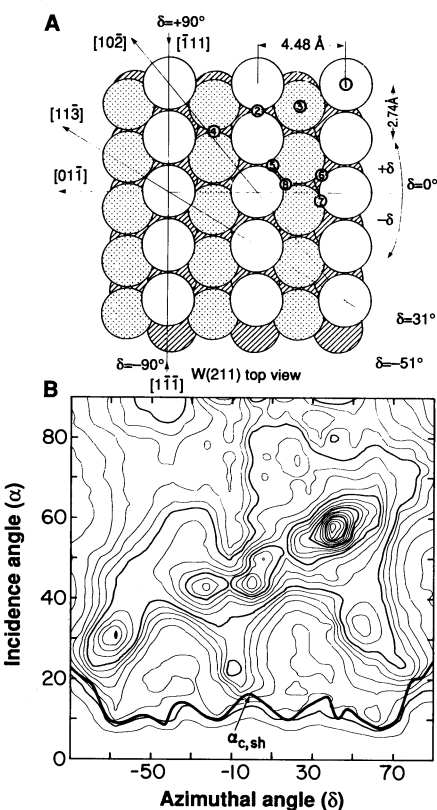


Fig. 5. (A) Structure of the bulk-truncated W(211) surface illustrating geometrically different adsorbate sites. Open circles, first-layer atoms; dotted circles, second-layer atoms; dashed circles, third- and fourth-layer atoms. **(B)** Scattering structural contour map (SSCM) for the clean W(211) surface. Contours of equal scattering intensity $I(S)$ are plotted as a function of α and δ . The critical value of α for first-layer scattering, $\alpha_{c,sh}^1$, is indicated.

Fig. 6. $I(FS)$ versus azimuthal angle δ for Pt(110) in the (1×2) missing-row reconstruction using Ar^+ at $\alpha = 5^\circ$ and $\theta = 40^\circ$, illustrating the surface periodicity.

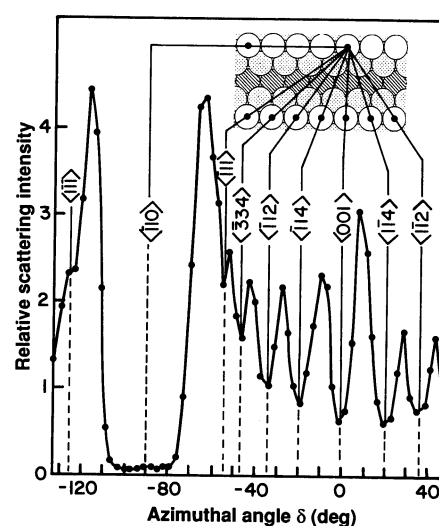
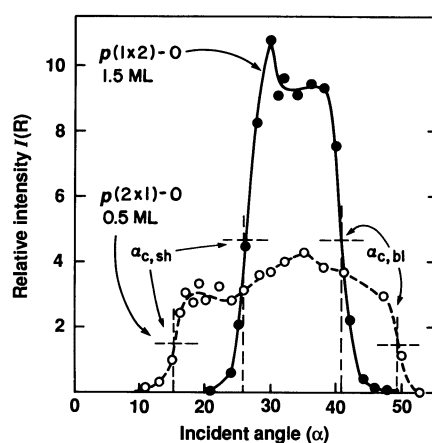


Fig. 7. Representative plots of $I(R)$ versus α for both high (1.5 ML) and low (0.5 ML) O coverages on a W(211) surface.



of the adsorbate atom relative to its nearest neighbors from p and the shape of the shadow cone.

Example plots of O $I(R)$ versus α for two different chemisorbed O coverages on W(211) are shown in Fig. 7. Low-dose exposure forms a $p(2 \times 1)$ structure consisting of 0.5 ML coverage and high-dose exposure forms a $p(1 \times 2)$ structure consisting of 1.5 ML coverage. The notation $(n \times m)$ defines the ratio of the lengths of the surface and substrate unit cells. Sharp rises in $I(R)$ appear at low α , and sharp decreases appear at high α . The rises are due to peaking of the ion flux at the edges of the shadow cones of neighboring atoms, and the decreases are due to blocking of recoil trajectories by neighboring atoms.

The critical α values for both shadowing, $\alpha_{c,sh}$, and blocking, $\alpha_{c,bl}$, can be used to determine interatomic spacings. At high coverage, $\alpha_{c,sh} = 24^\circ$ and $\alpha_{c,bl} = 42^\circ$, which are considerably higher and lower, respectively, than the values $\alpha_{c,sh} = 16^\circ$ and $\alpha_{c,bl} = 48^\circ$ obtained at low coverage. This indicates that, as O coverage increases, both the shadowing and blocking effects are enhanced as a result of close packing of O atoms along this azimuth; this results from shadowing and blocking of O atoms by their neighboring O atoms. The $\alpha_{c,sh}$ and $\alpha_{c,bl}$ values correspond to O atoms separated by a distance of two W lattice constants at low coverage and one W lattice constant at high coverage.

Recoiling structural contour map (RSCM). Plots of O $I(R)$ versus δ are symmetrical about $\delta = 0^\circ$, indicating that the O atoms occupy positions that are symmetrical about the $[01\bar{1}]$ azimuth. Plotting the $I(R)$ data in α, δ -space provides a recoiling structural contour map as shown in Fig. 8. This RSCM is a fingerprint for O atoms on the

W(211) surface. The symmetry about $\delta = 0^\circ$ eliminates the asymmetrical sites 3, 4, 6, 7, and 8 of Fig. 5. Comparison of $I(\text{BS})$ for the clean and O-covered surface indicates that only site 5, the threefold site in which the O atom is bound to two first- and one second-layer W atoms, is consistent with all of the experimental data. The O-W bond lengths, determined from detailed analysis (24, 26), are 1.83 Å and 2.17 Å to the first- and second-layer W atoms, respectively.

Hydrogen on the W(211) surface. The H RSCM in Fig. 8 exhibits only one $\alpha_{c,sh}$ value at low α , which is approximately constant at 4° for the region $-85^\circ < \delta < +85^\circ$ and increases to $\alpha_{c,sh} = 10^\circ$ for $\delta = \pm 90^\circ$. This indicates that the H is located in rather high positions above the surface and that close packing of H atoms occurs along the $\delta = \pm 90^\circ$ azimuths. A relatively flat region is observed in the center and background of the H RSCM, indicating that there is no H buried in subsurface layers that is accessible for recoiling at higher α . The symmetry of the RSCM about $\delta = 0^\circ$ arises from an adsorption site that is symmetrical with respect to the $[01\bar{1}]$ azimuth. The only H-atom positions that are consistent with all of the data are located within a band above the $[\bar{1}\bar{1}\bar{1}]$ troughs. Shadowing and blocking of H atoms along the $-85^\circ < \delta < +85^\circ$ directions is due to neighboring first-layer W atoms and along $\delta = \pm 90^\circ$ is due to neighboring H atoms. Observation (27) of H recoils with similar $\alpha_{c,sh}$ along all azimuths except $\delta = \pm 90^\circ$ suggests that the H atom positions are delocalized along the troughs rather than in localized sites. Detailed analysis shows that the H is confined to a band located at 0.58 Å above the troughs with an average H-H spacing equal to that of the W lattice. This result is in agreement with theoretical calculations (27, 28) of the electronic structure, which predict a broad probability distribution for the H-atom positions above the troughs due to thermally activated vibrational motion.

Ion-Surface Electron Exchange from TOF-SARS

Ion-surface electronic transition probabilities are determined by electron tunneling between the valence bands of the surface and the AOs of the ion. Such transition probabilities are highest for close distances of approach. An example of this is shown in Fig. 9 as a plot

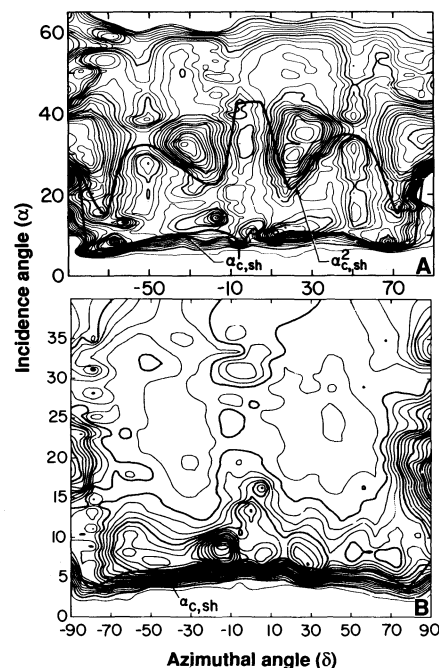


Fig. 8. Recoiling structural contour maps for the W(211)-p(1 × 2)-O (A) and W(211)-H (B) surfaces. Contours of equal recoiling intensity $I(\text{R})$ are plotted as a function of α and δ . Azimuths are defined as in Fig. 5. The critical shadowing angles, $\alpha_{c,sh}^i$, are indicated.

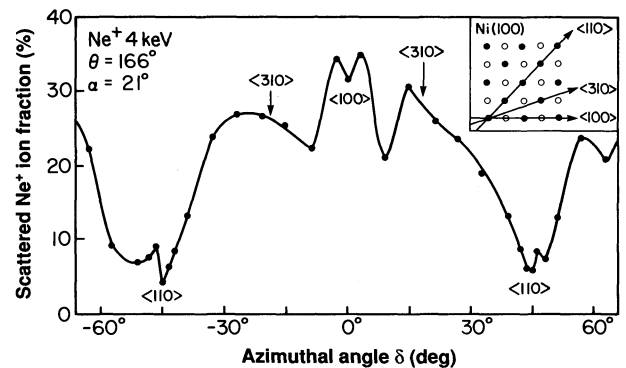


Fig. 9. Scattered Ne^+ ion fractions for 4-keV Ne^+ impinging on a Ni(100) surface as a function of azimuthal angle δ .

of the Ne^+ ion fraction, that is, $F = \text{ions}/(\text{neutrals} + \text{ions})$, scattered from a Ni(100) surface. The F is highest along the $[100]$ azimuth where scattering is only from the first layer (second-layer atoms are shadowed). The F is lowest along the $[110]$ azimuth where both first- and second-layer scatterings occur. The degree of neutralization is higher for second-layer scattering because the ion trajectories are close to several other atoms (both first- and second-layer ones). The symmetrical nature of the plot reflects the lattice periodicity. In general, low-scattered ion fractions F are observed when the ion trajectory goes through a region of high electron density near several atoms. Monitoring F at selected scattering geometries can serve as a probe of surface electron density.

New Developments in Scattering for Surface Structural Analysis

New developments in structural applications of ion scattering are occurring rapidly. Some examples of structures that have recently been solved through ion scattering and recoiling are as follows: O on TiC(111) (16), O on Fe(100) (15), H on Pt(997) (6), reconstruction of Ir(110) (7, 29) and Au(110) (8), As on Si(001) (9), O on Ni(110) (10), O and C on W(001) (11), NiAl(110) and (100) (12), Ag on Si(111) (13), and Au on Si(111) (14). Aono *et al.* (30) have recently demonstrated coaxial ion scattering in which the ion beam goes through a hole in a channel plate detector, allowing detection of 180° scattering. Because this apparatus fits on a single flange, it is suitable for in situ monitoring of epitaxial film growth of atomic layers and for time-resolved analysis of dynamical surface processes. Williams *et al.* (31) have recently developed fast programs for computer simulation of scattering processes. These programs are extremely valuable in solving unknown structures because they allow comparison of experimental data to simulations based on proposed structural models.

Role of TOF-SARS in the Myriad of Surface Science Techniques

The TOF-SARS technique contributes to our knowledge of surface science through (i) elemental analysis, (ii) structural analysis, and (iii) analysis of electron exchange probabilities. We will consider the merits of each of these three areas.

Elemental analysis. Although TOF-SARS is sensitive to all elements, including H, the limited resolution of the TOF technique presents difficulties in resolving spectral peaks of high-mass elements with similar masses. The unique feature for elemental analysis is direct monitoring of surface H. For general qualitative and quantita-

tive surface elemental analyses, XPS and AES remain the techniques of choice.

Structural analysis. The major role of TOF-SARS is as a technique for analyzing surface structure that is capable of probing the positions of all elements with an accuracy of ≤ 0.1 Å. TOF-SARS is sensitive to short-range order—individual interatomic spacings along azimuths. It provides a direct measure of interatomic distances in the first and subsurface layers and a measure of surface periodicity in real space. It is complementary to LEED, which probes long-range order and minimum domain size of 100 to 200 Å, and provides a measure of surface and adsorbate symmetry in reciprocal space. Coupling TOF-SARS and LEED provides a powerful combination for surface structure investigations. The techniques of medium- and high-energy (Rutherford backscattering) ion scattering sample subsurface and bulk structure and are not as surface-sensitive as TOF-SARS.

Ion-surface electron exchange probabilities. One of the unsolved problems in the interaction of low-energy ions with surfaces is the mechanism of charge transfer and prediction of the charge composition of the flux of scattered, recoiled, and sputtered atoms. The ability to collect spectra of neutrals plus ions and only neutrals provides a direct measure of scattered and recoiled ion fractions. Plots of ion fractions in α, δ -space provide electronic transition probability contour maps that are related to surface electron density along the various azimuths. Consistency between such electron density contours and the SSCMs provides a unique description of the surface electronic and atomic structure.

Conclusions and Future Developments

Emphasis in this article has been placed on the physical concepts and applications of TOF-SARS rather than on quantitative descriptions of the phenomena. Future experimental developments will include the use of large channel plates or hemispherical grids for spatial resolution of particles ejected through a large solid angle, facilitating rapid and direct collection of an entire scattering and recoiling structural map. Improvements in optics will provide narrower ion pulse widths, resulting in enhanced time resolution of the spectra. Development of the simulations will make computer

modeling of surface structures routine. TOF-SARS is now well established as a technique for surface structural analysis that will have a significant impact in areas as diverse as thin film growth, catalysis, H embrittlement and penetration of materials, surface reaction dynamics, and analysis of interfaces.

REFERENCES AND NOTES

1. W. K. Chu, J. W. Mayer, M. A. Nicolet, *Backscattering Spectrometry* (Academic Press, New York, 1978).
2. D. P. Smith, *J. Appl. Phys.* **38**, 340 (1967).
3. M. Aono *et al.*, *Jpn. J. Appl. Phys.* **21**, L670 (1982).
4. L. Marchut, T. M. Buck, G. H. Wheatley, C. J. McMahon, Jr., *Surf. Sci.* **141**, 549 (1984).
5. J. W. Rabalais, *CRC Crit. Rev. Solid State Mater. Sci.* **14**, 319 (1988).
6. B. J. Koel, S. T. de Zwart, A. L. Boers, B. Poelsema, I. K. Verheij, *Phys. Rev. Lett.* **56**, 1152 (1986).
7. W. Hetterich and W. Heiland, *Surf. Sci.* **210**, 129 (1989).
8. H. Derks, J. Möller, W. Heiland, *ibid.* **188**, L685 (1987).
9. H. Niehus, K. Mann, B. N. Eldridge, M. L. Yu, *J. Vacuum Sci. Technol. A* **6**, 625 (1988).
10. D. J. O'Connor, *Surf. Sci.* **173**, 593 (1986).
11. D. R. Mullins and S. H. Overbury, *ibid.* **210**, 481 (1989); *ibid.*, p. 501.
12. ———, *ibid.* **199**, 141 (1988).
13. C. S. Chang, T. L. Porter, I. S. T. Tsong, *J. Vacuum Sci. Technol. A* **7**, 1906 (1989).
14. J. H. Huang and R. S. Williams, *Phys. Rev. B* **38**, 4022 (1988).
15. J. M. Van Zoest, J. M. Fluit, T. J. Vink, B. A. Van Hassel, *Surf. Sci.* **182**, 179 (1987).
16. R. Souda, C. Oshima, S. Otani, Y. Ishizawa, M. Aono, *ibid.* **199**, 154 (1988).
17. E. S. Mashkova and V. A. Molchanov, *Medium-Energy Ion Reflection from Solids* (North-Holland, Amsterdam, 1985).
18. J. F. Zeigler, J. P. Biersack, U. Littmark, *The Stopping and Range of Ions in Solids* (Pergamon, New York, 1985).
19. O. S. Oen, *Surf. Sci.* **131**, L407 (1983).
20. C. S. Chang, U. Knipping, I. S. T. Tsong, *Nucl. Instrum. Methods Phys. Res. B* **18**, 11 (1986); *ibid.* **35**, 151 (1988).
21. S. R. Kasi, H. Kang, C. S. Sass, J. W. Rabalais, *Surf. Sci. Rep.* **10**, 1 (1989).
22. O. Grizzi, M. Shi, H. Bu, J. W. Rabalais, *Rev. Sci. Instrum.* **61**, 740 (1990).
23. H. Niehus, *Surf. Sci.* **145**, 407 (1984).
24. J. W. Rabalais, O. Grizzi, M. Shi, H. Bu, *Phys. Rev. Lett.* **63**, 51 (1989).
25. O. Grizzi, M. Shi, H. Bu, J. W. Rabalais, P. Hochmann, *Phys. Rev. B* **40**, 10127 (1989).
26. H. Bu, O. Grizzi, M. Shi, J. W. Rabalais, *ibid.*, p. 10147.
27. M. Shi *et al.*, *ibid.*, p. 10163.
28. O. Grizzi *et al.*, *Phys. Rev. Lett.* **63**, 1408 (1989).
29. H. Bu, M. Shi, F. Masson, J. W. Rabalais, *Surf. Sci. Lett.* **230**, L140 (1990).
30. M. Aono *et al.*, *Nucl. Instrum. Methods Phys. Res. B* **37/38**, 264 (1989).
31. R. S. Williams, M. Kato, R. S. Daley, M. Aono, *Surf. Sci.* **225**, 355 (1990).
32. I thank all of the members of my research group and particularly H. Bu, O. Grizzi, C. C. Hsu, F. Masson, and M. Shi for their contributions to this work. Supported by the National Science Foundation and the R. A. Welch Foundation.